



Solid-phase hot-pressing of POMs-ZIFs precursor and derived phosphide for overall water splitting

Yu-Jia Tang, Hong-Jing Zhu, Long-Zhang Dong, A-Man Zhang, Shun-Li Li, Jiang Liu*, Ya-Qian Lan*

Jiangsu Collaborative Innovation Centre of Biomedical Functional Materials, Jiangsu Key Laboratory of New Power Batteries, School of Chemistry and Materials Science, Nanjing Normal University, Nanjing, 210023, China

ARTICLE INFO

Keywords:

Hot-pressing
Phosphide
Metal-organic framework
HER
OER

ABSTRACT

Rational design of electrocatalyst with high performance for both hydrogen and oxygen evolution reaction is attracting considerable attention in recent years. However, most electrocatalysts are powders and require to deposit on conductive substrates with binders, leading to complicated steps and hindering the improvement of long-term stability. This work exhibits a solid-phase hot-pressing method to prepare polyoxometalates based zeolitic imidazolate frameworks (POMs-ZIFs) precursor on carbon cloth (CC) rapidly and mildly. After phosphidation treatment, nitrogen-doped graphitic carbon layers coated phosphide on CC (CoP/MoP@NC/CC) is synthesized. CoP/MoP@NC/CC has excellent electrocatalytic performance for water splitting due to the synergistic effect of CoP, MoP and as-formed oxide/hydroxide layers. It shows the low overpotentials of 94 mV for HER and 270 mV for OER at the current density of 10 mA cm^{-2} in alkaline medium, which is superior to most of the reported phosphide-based electrocatalysts. Notably, the ultra-high current density of 1000 mA cm^{-2} can be reached at the overpotentials of only 475 mV for HER and 657 mV for OER. As both cathode and anode for overall water splitting, CoP/MoP@NC can achieve the current density of 50 mA cm^{-2} at the cell voltage of 1.71 V. The solid-phase hot-pressing method ensures the tight and uniform growth of the fast nucleating and stable materials on substrate and applies for more electrochemical reactions.

1. Introduction

Hydrogen (H_2) has been widely recognized as the most promising and sustainable energy source in place of the carbon-based fuels [1,2]. However, major production of H_2 is still made from the conventional methods, such as the steam reforming, which accompany with the generation of carbon dioxide (CO_2) to affect the environment [3,4]. Electrochemical water splitting is a non-polluting technique to produce H_2 and oxygen (O_2) through hydrogen evolution reaction (HER) and oxygen evolution reaction (OER), respectively [5–7]. Currently, commercial noble-metal-based materials (e.g., Pt/C, IrO_2) are the state-of-the-art electrocatalysts to promote the kinetically sluggish water splitting reaction efficiently [8,9]. However, the industrial application is restricted owing to their high cost and scarceness. Therefore, the robust noble-metal-free electrocatalysts, especially the transition metal-based composites (e.g., sulfides, [10–14] oxides [15,16], phosphides [17,18] and hydroxides [19–21]), with low cost and high activity are urgently needed to lower the activation barrier for water splitting.

Transition metal phosphides (TMPs) have received considerable

attention and investigation for the electrolysis of water because of the similar zero-valent metallic character [22]. In particular, phosphide-based composites are supposed to be more favorable and active after introducing a secondary transition metal into the monometallic phosphide system to tailor the electronic structure and surface property [23]. Recently, TMPs are reported as the efficient HER or OER electrocatalysts, such as Ni_2P , [24] $\text{Fe}_{1.1}\text{Mn}_{0.9}\text{P}$, [25] CoP [26], $\text{Co}_3\text{Ni}_1\text{P}$, [27] Ni-Cu-P [28] and so on. However, TMP-based electrocatalysts, especially for OER, are unstable and prone to corrosion at the high overpotential and in the strong alkaline medium. Therefore, hybridizing TMPs with porous carbon materials can be an effective way to improve the corrosion resistance and the long-term stability for water splitting [29].

Metal-organic frameworks (MOFs) are the classic crystalline materials that metal ion/cluster can be bridged by organic ligand to form the periodic porous structure [30,31]. MOFs have been reported as the popular precursors to synthesize porous carbon-based nanomaterials with controllable compositions and morphologies in energy conversion and storage applications [32–35]. In this regard, MOFs as

* Corresponding authors.

E-mail addresses: liuj@njnu.edu.cn (J. Liu), yqlan@njnu.edu.cn (Y.-Q. Lan).

<https://doi.org/10.1016/j.apcatb.2019.01.007>

Received 6 October 2018; Received in revised form 30 December 2018; Accepted 4 January 2019

Available online 06 January 2019

0926-3373/ © 2019 Elsevier B.V. All rights reserved.

phosphidation precursors can prepare TMP particles encapsulated in heteroatom-doped porous carbon, which can avoid the structural damage and property deterioration during the electrolysis measurement. For example, Wang et al. reported a bi-functional $\text{Cu}_3\text{P@NPPC}$ electrocatalyst for both HER and oxygen reduction reaction (ORR) [36]. N, P-doped porous carbon shell for Cu_3P nanoparticles derived from Cu-based MOF can provide the protection to enhance the related performance and long-term durability. Therefore, MOFs can be the ideal precursors for synthesizing TMP-based composites, which can avoid corrosion and improve the catalytic performance simultaneously.

Up to now, most MOF-derived nanomaterials are powders and require to load on conductive substrates (e.g., glassy carbon electrode and nickel foam) with Nafion [37,38]. However, the loading amount and testing area are limited due to the fixed area of the traditional substrates. Catalysts are easy to peel off from the substrates during the measurement, thus decreasing the activity. Moreover, hydrothermal method is usually applied to synthesize MOFs with disadvantages of high energy consumption, long reaction time, solvent contamination and so on. If a simple and mild strategy is applied to *in situ* synthesize MOFs on the conductive substrates, we can resolve the above problems well for fast preparation of MOF-based composites in quantity. The subsequent MOF-derived nanomaterials can be directly served as the working electrodes with adjustable loadings and areas for water electrolysis. Therefore, exploring an ingenious method for the preparation of MOFs and their derivatives on substrates tightly and uniformly still remains a great challenge.

Herein, a facile and rapid solid-phase hot-pressing method is utilized to synthesize a polyoxometalate-based MOF and their derived phosphide on carbon cloth (CC) successfully. The solid-phase hot-pressing method has many advantages of solvent-free, non-pollution, high yield and fast nucleation [39]. As the classic MOFs, zeolitic imidazolate frameworks (ZIFs) chosen here possess unique 3D zeolite-like topological structure, abundant carbon and nitrogen sources from the ligand as well as the fast nucleation feature. ZIFs can be carbonized to synthesize the well-known nitrogen-doped porous carbon nanocomposites (M-N-C), which are able to tune the electronic structure and electrocatalytic activity for ZIF-derived nanomaterials [40,41]. However, the optional metal sources (*i.e.*, Zn, Co) from ZIFs are limited thus giving the monometallic phosphides. Notably, polyoxometalates (POMs) are the metal-oxygen clusters with abundant transition metal sources (e.g., Mo, W, V) [42]. POMs have been widely used to synthesize the efficient Mo or W-based electrocatalysts for water splitting [43–46]. In this regard, POMs coupled with ZIFs (POMs-ZIFs) can be hot-pressed on CC as precursor to prepare phosphide with unique structure and large surface area [47]. In this work, Keggin-type POMs of PMo_{12} coupled with Co/Zn ZIFs ($\text{PMo}_{12}\text{-Co/Zn-ZIFs}$) are hot-pressed on CC using the isomorphous ZIF-67 and ZIF-8 with Co/Zn molar ratio of 1:1. Then nitrogen-doped graphitic carbon coated phosphide on CC (CoP/MoP@NC/CC) is fabricated through the phosphidation of $\text{PMo}_{12}\text{-Co/Zn-ZIFs/CC}$. As the bi-functional electrode for water splitting, CoP/MoP@NC exhibits the low overpotentials of 94 mV for HER and 270 mV for OER at 10 mA cm^{-2} , respectively, which is one of the best electrocatalysts among most reported phosphide-based composites to date. For overall water splitting, CoP/MoP@NC as both cathode and anode can achieve the current density of 50 mA cm^{-2} at the cell voltage as low as 1.71 V.

2. Material and methods

2.1. Chemicals

Zinc acetate dihydrate ($\text{Zn(OAc)}_2 \cdot 2\text{H}_2\text{O}$, AR), cobalt nitrate hexahydrate ($\text{Co(NO}_3)_2 \cdot 6\text{H}_2\text{O}$, AR), phosphomolybdic acid ($\text{H}_3\text{PMo}_{12}\text{O}_{40} \cdot \text{nH}_2\text{O}$, PMo_{12} , AR), 2-methylimidazole ($\text{C}_4\text{H}_6\text{N}_2$, $\geq 99\%$, AR), red phosphorus (P, AR), nitric acid (HNO_3 , 65–68%, AR) and ethylene glycol ($\text{C}_2\text{H}_6\text{O}_2$, EG, AR) were purchased from Sinopharm

Chemical Reagent Co., Ltd. Polyethylene glycol ($\text{HO(CH}_2\text{CH}_2\text{O)}_n\text{H}$, PEG, MW. 4000) was bought from Aladdin Industrial Corporation. 20% Pt/C, IrO_2 and Nafion solution (5 wt%) were bought from Sigma-Aldrich. Carbon cloth (WOS1002) was purchased from CeTech Co., Ltd.

2.2. Preparation of $\text{PMo}_{12}\text{-Co/Zn-ZIFs/CC}$ precursor

Carbon cloth (CC) with the size of $1 \times 2\text{ cm}^2$ was treated by the concentrated nitric acid to remove the residual organic species. $\text{Zn(OAc)}_2 \cdot 2\text{H}_2\text{O}$ (0.11 g, 0.5 mmol), $\text{Co(NO}_3)_2 \cdot 6\text{H}_2\text{O}$ (0.15 g, 0.5 mmol), 2-methylimidazole (0.5 g), PMo_{12} (0.1 g, 0.055 mmol) and 0.1 g PEG were added together into a mortar with four drops of EG. The mixture was grinded to form the purple viscous paste. The paste was coated onto both sides of CC and then wrapped with the aluminum foil. The electric iron was used to hot-press the samples for both sides at ca. 150°C for 20 min. After peeling off the aluminum foil, $\text{PMo}_{12}\text{-Co/Zn-ZIFs/CC}$ was obtained. In contrast, Co/Zn-ZIFs/CC and $\text{PMo}_{12}\text{-ZIF-8/CC}$ were hot-pressed without PMo_{12} and $\text{Co(NO}_3)_2 \cdot 6\text{H}_2\text{O}$, respectively.

2.3. Preparation of CoP/MoP@NC/CC

Two pieces of $\text{PMo}_{12}\text{-Co/Zn-ZIFs/CC}$ were placed in a ceramic boat with 0.4 g red phosphorous at the upstream side of a horizontal tube furnace. The furnace was heated to 400°C at 5°C min^{-1} for 2 h and then up to 900°C for another 3 h under the nitrogen flow (N_2 , 99.999%). Afterwards, the furnace was cooled down to the room temperature to obtain CoP/MoP@NC/CC . The loading mass of CoP/MoP@NC on CC was ca. 0.8 mg cm^{-2} . Contrast samples of CoP@NC/CC and MoP@NC/CC were carbonized using Co/Zn-ZIFs/CC and $\text{PMo}_{12}\text{-ZIF-8/CC}$ precursors, respectively.

2.4. Material characterization

Powder X-Ray diffraction (PXRD) patterns were recorded on a D/max 2500 VL/PC diffractometer (Japan) equipped with graphite monochromatized Cu $\text{K}\alpha$ radiation ($\lambda = 1.54060\text{ \AA}$). Corresponding work voltage and current is 40 kV and 100 mA, respectively. Transmission electron microscopy (TEM) and high-resolution TEM (HRTEM) images were carried out on JEOL-2100 F apparatus at an accelerating voltage of 200 kV. Morphology and microstructure analysis was conducted using a scanning electron microscope (SEM, JSM-7600 F) at an acceleration voltage of 10 kV. Energy dispersive X-ray spectroscopy (EDX) was performed with JSM-5160LV-Vantage typed energy spectrometer. X-ray photoelectron spectroscopy (XPS) was collected on scanning X-ray microprobe (PHI 5000 Versa, ULAC-PHI, Inc.) using Al $\text{K}\alpha$ radiation and the C 1s peak at 284.8 eV as internal standard. N_2 adsorption/desorption isotherms were conducted at 77 K using a quantachrome instrument.

2.5. Electrochemical measurement

HER and OER performance of CoP/MoP@NC/CC was tested on an electrochemical workstation (Bio-Logic, SP-150) with a typical three-electrode setup in N_2 -saturated 1 M KOH. CoP/MoP@NC/CC was used as the direct working electrode, while graphite rod and saturated calomel electrode (SCE) were used as the counter and reference electrode, respectively. The measurement area is 0.25 cm^2 . All the polarization curves were used by 85% *iR* correction. The potential (vs. SCE) was transferred to the reversible hydrogen electrode (RHE) by the following equation: $E_{\text{RHE}} = E_{\text{SCE}} + 1.07\text{ V}$. LSV curves were performed at the scan rate of 2 mV s^{-1} . Tafel slopes were calculated according to the Tafel equation: $\eta = \text{blog}j + a$. The chronoamperometry (CA) was conducted at the overpotential of 150 mV for HER and 300 mV for OER for 20 h. EIS was carried out at the overpotential of 150 mV for HER and 300 mV for OER in the frequency range from 1000 to 10 mHz with an AC amplitude of 10 mV. C_{dl} was calculated according to CV curves obtained at

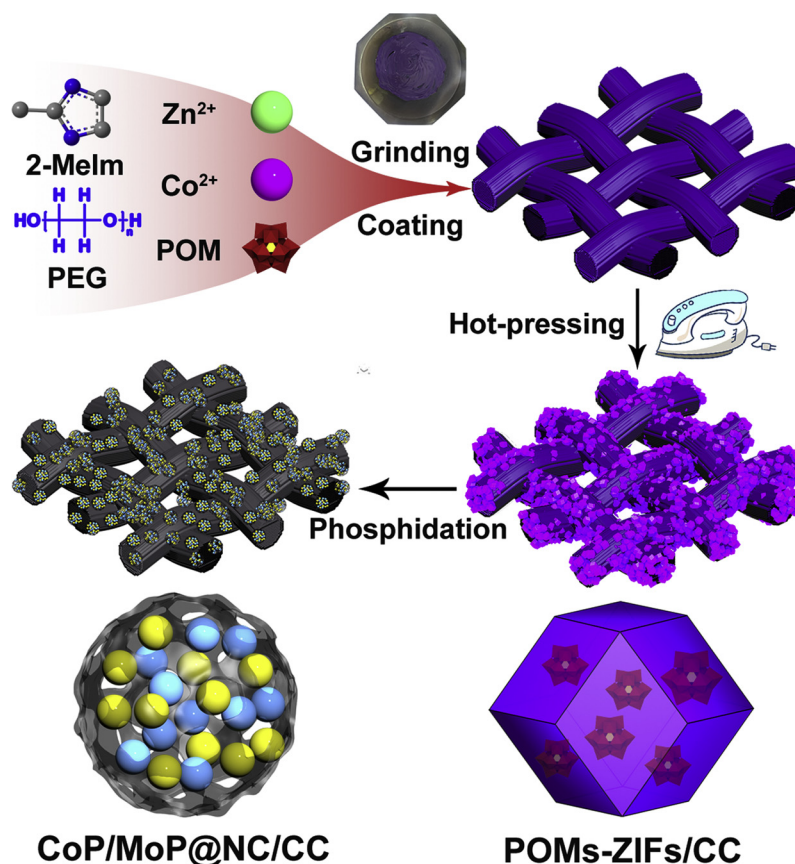


Fig. 1. The illustration of the preparation process of CoP/MoP@NC/CC.

different scan rates (20, 40, 60, 80 and 100 mV s⁻¹) from -0.6 to -0.5 V vs. SCE in 1 M KOH.

3. Results and discussion

3.1. Structural and morphological characterization

The synthesis process of POMs-ZIFs precursor and the derived phosphide is illustrated in Fig. 1. In brief, PMo₁₂, zinc acetate (Zn (Ac)₂), cobalt nitrate (Co(NO₃)₂), 2-methylimidazole and polyethylene glycol (PEG) with few drops of ethylene glycol (EG) were grinded together to form the purple pastes. Then the pastes were coated on CC and hot-pressed using an electric iron under the mild temperature (ca. 150 °C) and the normal pressure to form PMo₁₂-Co/Zn-ZIFs/CC precursor. After phosphidation of PMo₁₂-Co/Zn-ZIFs/CC in the flowing N₂ atmosphere with red phosphorus in the upstream, CoP/MoP@NC/CC can be obtained.

Powder X-ray diffraction pattern (PXRD) was firstly used to analyze the composition of precursor and derived phosphide on CC. PXRD spectrum of PMo₁₂-Co/Zn-ZIFs/CC precursor (Figure S1) is matched well with the simulated isomorphous ZIF-8 or ZIF-67, suggesting the successful hot-pressing of POMs-ZIFs composite with crystallized structure [48]. Contrast samples of Co/Zn-ZIFs/CC and PMo₁₂-ZIF-8/CC precursors are also synthesized successfully according to PXRD analysis (Figure S1). After phosphidation, PXRD spectrum of CoP/MoP@NC/CC (Fig. 2a) displays two different components of CoP (JCPDS No. 29-497) and MoP (JCPDS No. 24-771). The peaks at 31.6, 36.3, 46.4, 48.3 and 56.7° can be assigned to the (011), (111), (112), (211) and (301) lattice planes of simulated CoP, while peaks at 32.2, 43.2 and 57.5° are in accord with the (100), (101) and (110) lattice planes of MoP. There are no characteristic peaks for Zn element because Zn can be evaporated (boiling point 907 °C) during the high

temperature treatment. In addition, the broad peak at 26° refers to the typical porous carbon derived from ZIFs and CC substrate. Contrast sample of CoP@NC/CC shows the main composition of CoP while MoP@NC/CC has the individual phosphide of MoP (Figure S2).

The morphology and structure of CoP/MoP@NC/CC were then characterized by scanning electron microscopy (SEM) and transmission electron microscopy (TEM) carefully. Typical SEM images of CoP/MoP@NC/CC at high and low magnifications (Fig. 2b) show uniform and dense nanoparticles with the size of ca. 100 nm on every carbon fiber tightly. TEM image of CoP/MoP@NC composite sonicated from CC (Fig. 2c) demonstrates the well-dispersed metal particles coated by the porous carbon. In comparison, SEM (Figure S3) and TEM (Figure S4) images of CoP@NC/CC and MoP@NC/CC exhibit the unevenly distributed agglomerates with varying sizes, further proving the importance of the combination of PMo₁₂ and ZIFs in precursor. HRTEM image (Fig. 2d) of CoP/MoP@NC reveals that phosphide nanoparticles are surrounded by several graphitic porous carbon layers (ca. 3–5 layers). The spacing of these carbon layers (0.34 nm) is consistent with the interlayer spacing of graphite. Moreover, there are two kinds of the obvious lattice fringes with the spacing value of 0.189 and 0.210 nm, assigning to the (211) lattice plane of CoP and the (101) plane of MoP, respectively. CoP/MoP@NC was then observed by the high-angle annular dark-field (HAADF) image (Fig. 2e). The corresponding element mappings show the existence of Co, Mo, P, N and C, confirming the formation of unique structure with metal particles encapsulated in the graphitic N-doped carbon layers. Energy dispersive X-ray (EDX) spectrum of CoP/MoP@NC/CC (Figure S5) also shows the existence of Co, Mo and P elements but no Zn, suggesting the successful preparation through phosphidation process.

N₂ adsorption/desorption analysis of CoP/MoP@NC/CC, CoP@NC/CC and MoP@NC/CC is shown in Figure S6. The Brunauer-Emmett-Teller (BET) surface area of the three samples is 82.4, 57.2 and

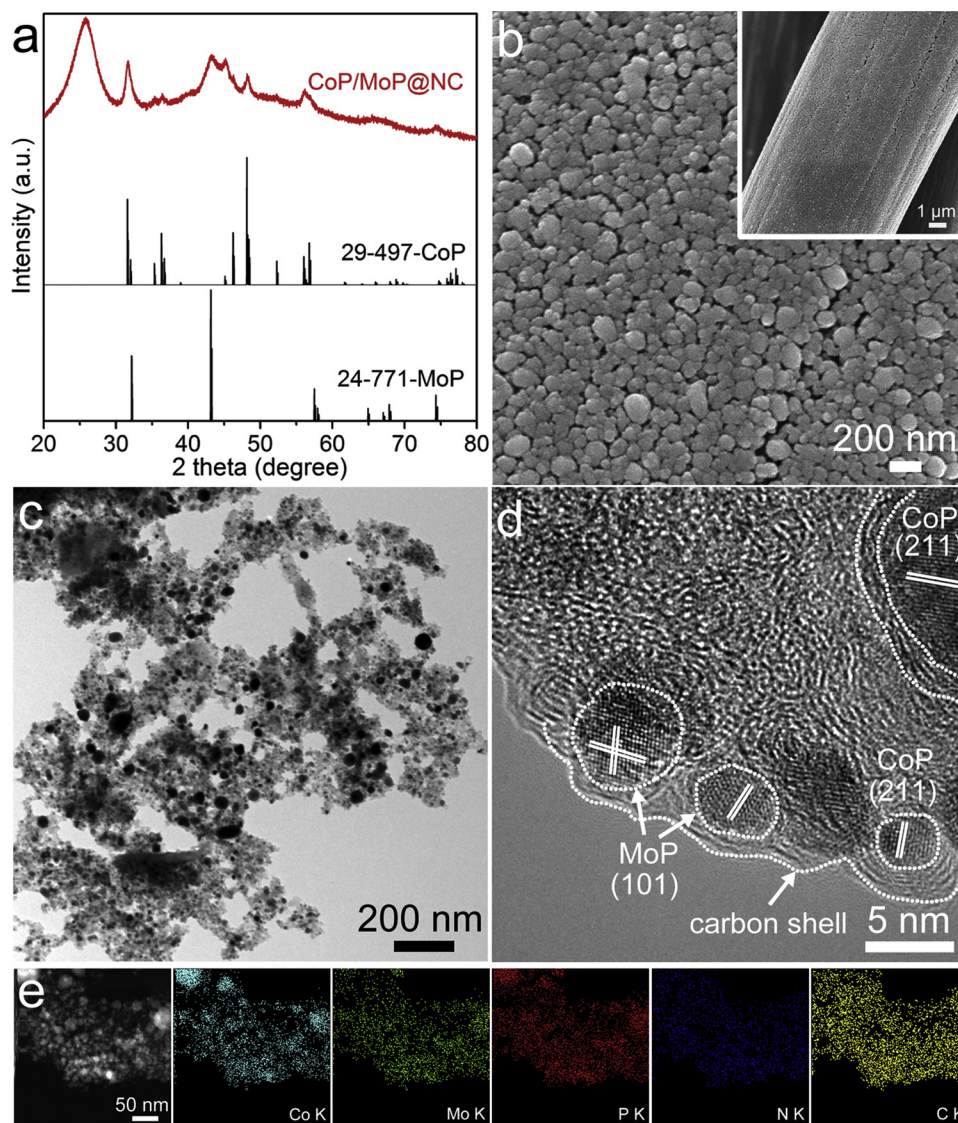


Fig. 2. (a) PXRD spectrum of CoP/MoP@NC on CC. (b) SEM images of CoP/MoP@NC on CC at high magnification and inset at low magnification. (c) TEM and (d) HRTEM images of CoP/MoP@NC sonicated from CC. (e) HAADF image and corresponding element mappings of CoP/MoP@NC.

$55.7 \text{ m}^2 \text{ g}^{-1}$, respectively. Quenched solid density functional theory (QSDFT) analysis demonstrates that the pore sizes are mainly concentrated from 2 to 30 nm. Remarkably, CoP/MoP@NC/CC has both micropores and mesopores ranging from 1.83 to 30 nm, the total pore volume of $9.56 \times 10^{-2} \text{ cm}^3 \text{ g}^{-1}$ and the micropore volume of $2.71 \times 10^{-3} \text{ cm}^3 \text{ g}^{-1}$. The high surface area and rich pore structure of CoP/MoP@NC/CC are caused by the uniform particle morphology and Zn evaporation from ZIF-8. Combining the above characterization results, the introduction of ZIF-8 not only ensures the successful preparation of $\text{PMo}_{12}\text{-Co/Zn-ZIFs}$ precursor but also increases the surface area after remove of Zn. Therefore, CoP/MoP@NC composite can be suitable for electrolyte to get to the accessible active sites rapidly in water electrolysis system.

The chemical compositions of CoP/MoP@NC/CC were further investigated by X-ray photoelectron spectroscopy (XPS). The full-scan spectrum (Figure S7) suggests the existence of C, O, N, P, Co and Mo, and the element percent is listed in Table S1. The high-resolution Co 2p spectrum (Fig. 3a) exhibits two main regions of Co $2p_{1/2}$ and Co $2p_{3/2}$ with ca. 15 eV binding energy difference. In Co $2p_{1/2}$ region, it can be deconvoluted into two peaks of Co^{2+} at 798.5 eV and the corresponding shake-up satellite peak at 803.8 eV. Similarly, Co $2p_{3/2}$ region demonstrates two peaks of Co^{2+} (782.9 eV) and Co^{3+} (779.2 eV) along

with the satellite peak at 786.6 eV. The two satellite peaks are assigned to the shakeup excitation of the high-spin Co^{2+} ions [49]. The Mo 3d spectrum in Fig. 3b can be fitted into six pairs of peaks. The peaks at 231.6 and 228.4 eV are in consistent with the binding energies of $\text{Mo}\delta^+$ $3d_{3/2}$ and $\text{Mo}\delta^+$ $3d_{5/2}$ for MoP. Besides, the peaks at 236.4 and 233.4 eV are assigned to Mo^{6+} $3d_{3/2}$ and Mo^{6+} $3d_{5/2}$ while the peaks located at 232.8 and 228.9 eV are Mo^{4+} $3d_{3/2}$ and Mo^{4+} $3d_{5/2}$, respectively. The existence of Mo^{4+} and Mo^{6+} suggests the partial surface oxidation in the air to form MoO_x species. The P 2p spectrum (Fig. 3c) exhibits two characteristic peaks of P $2p_{1/2}$ and P $2p_{3/2}$ at 130.4 and 129.7 eV, respectively, which further proves the successful preparation of phosphide on CC. The relatively strong peak at 134.4 eV is referred to P–O bond due to the oxidized phosphates. N 1s spectrum (Fig. 3d) reveals the presence of four types of N species including pyridinic N (398.4 eV), pyrrolic N (399.6 eV), graphitic N (401.3 eV) and oxidized N (402.4 eV).

3.2. Electrocatalytic performance

To eliminate the influence of the substrates, linear sweep voltammetry (LSV) curves and Tafel slopes of bare CC for HER and OER were firstly tested in 1 M KOH (Figure S8). CC shows poor water splitting

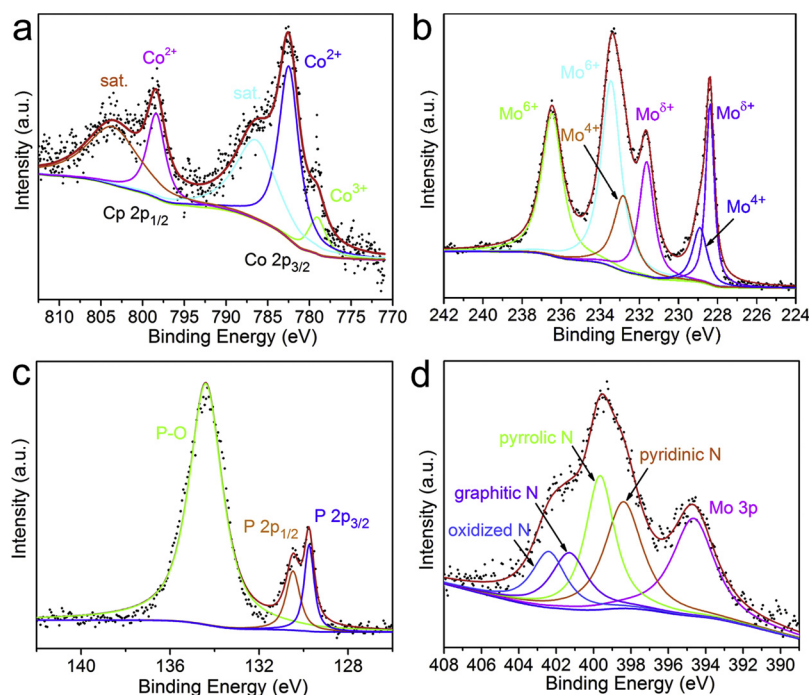


Fig. 3. High-resolution XPS spectra of CoP/MoP@NC on CC: (a) Co 2p, (b) Mo 3d, (c) P 2p and (d) N 1s.

performance with large onset overpotential and small current density. In order to screen out the optimum preparation condition of catalyst as cathode and anode separately, HER and OER properties of CoP/MoP@NC composite with different P_{Mo} loadings (0.04, 0.10 and 0.15 g) and Co/Zn molar ratios (1:1, 1:2 and 2:1) in precursor are compared. LSV curves and Tafel slopes in Figure S9 suggest that CoP/MoP@NC prepared with 0.10 g POMs possesses the best HER and OER activity. The performance of CoP/MoP@NC with different Co/Zn molar ratios in precursor is also compared in Figure S10. When P_{Mo} loading is fixed to 0.10 g, the optimal Co/Zn molar ratio is 1:1. Moreover, CoP/MoP@NC is prepared at different phosphidation temperatures (900 and 1000 °C) and times (2, 3 and 4 h) (Figure S11 and S12). 900 °C as well as 3 h are selected as the best carbonization condition.

3.2.1. HER performance of CoP/MoP@NC/CC

The HER performance of CoP/MoP@NC/CC as direct working electrode was evaluated using a typical three-electrode system in N₂-saturated 1 M KOH. The contrast samples of CoP@NC/CC, MoP@NC/CC and commercial 20% Pt/C on CC are also measured. In Fig. 4a, LSV curve of CoP/MoP@NC exhibits a very low onset overpotential of ca. 37 mV vs. RHE following with the rapid increasing current density. By contrast, CoP@NC and MoP@NC demonstrate more negative onset overpotentials of ca. 70 and 120 mV vs. RHE while 20% Pt/C has the lowest onset overpotential of 0 mV. Tafel plots (Fig. 4b) are carried out to analyze the kinetic process. Except for commercial 20% Pt/C (38 mV dec⁻¹), Tafel slopes of CoP/MoP@NC, CoP@NC and MoP@NC are 40, 85 and 52 mV dec⁻¹, respectively, occurring in the Volmer-Heyrovsky pathway. The overpotential achieved at the current density 10 mA cm⁻² (η_{10}) is a crucial parameter to evaluate the performance of the electrocatalyst. Fig. 4c compares η_{10} of the as-prepared samples using a histogram. η_{10} of CoP/MoP@NC is only 94 mV vs. RHE, which is much lower than the contrast samples (i.e., CoP@NC, 157 mV and MoP@NC, 200 mV). Furthermore, the low η_{10} and Tafel slope of CoP/MoP@NC also outperform most of the recently reported phosphide-based composites for HER, such as Ni₂P-CoP [50] (η_{10} , 105 mV; Tafel slope, 64 mV dec⁻¹), Cu_{0.3}Co_{2.7}P/NC [51] (η_{10} , 220 mV; Tafel slope, 122 mV dec⁻¹) (Table S2).

The long-term stability is another criterion to access HER activity of

electrocatalysts. In Fig. 4d, CoP/MoP@NC composite shows the remarkable stability for HER in alkaline electrolyte. LSV curves at the initial as well as after 1000 and 5000 cyclic voltammetry (CV) cycles are almost overlapped even reaching the ultra-high current density of 1000 mA cm⁻² at the overpotential of 475 mV vs. RHE. There is only 7 mV negative shift at -10 mA cm⁻² before and after 5000 CV cycles. In addition, chronopotentiometric (CA) curve (inset in Fig. 4d) shows negligible decrease with the current density of ca. -15 mA cm⁻² measured at a constant overpotential of 150 mV for more than 20 h, indicating the excellent long-term durability. It is worth mentioning that there are still few reports for water splitting electrocatalysts, which can get to such high level of the current density at the relatively low overpotential [52].

The electrochemical impedance spectroscopy (EIS) is then taken into account for HER activity analysis. EIS spectrum of CoP/MoP@NC (Fig. 4e) has a small semicircle at the high frequency region assigning to the charge transfer resistance (R_{ct}), suggesting the favorable electronic/ionic transfer at the electrolyte/electrode interface. According to the fitting result, R_{ct} of CoP/MoP@NC (1.9 Ω) is much lower than that of CoP@NC (8.1 Ω) and MoP@NC (14.0 Ω), which is resulting from the high conductivity and the fast charge transfer ability when coupling with two phosphide components. The electrochemical active surface area (ECSA) is also used to prove their different HER performance, which can be measured by electrochemical double layer capacitance (C_{dl}). CV curves of CoP/MoP@NC, CoP@NC, MoP@NC tested at different scan rates (20–100 mV s⁻¹) in the non-faradic potential region are shown in Figure S13. Fig. 4f is the plots of the difference between the anode and cathode current density (Δj) against the different scan rates. According to the calculated slope, CoP/MoP@NC has a higher C_{dl} value of 223 mF cm⁻² than that of CoP@NC (158 mF cm⁻²) and MoP@NC (22 mF cm⁻²), revealing its high ECSA. This is because CoP/MoP@NC on CC has larger surface area and more exposed active sites than the monometallic phosphides. In this regard, CoP/MoP@NC composite shows the superior HER activity than the contrast samples due to the synergistic effect of MoP and CoP.

3.2.2. OER performance of CoP/MoP@NC/CC

As another half reaction of water electrolysis, OER also requires

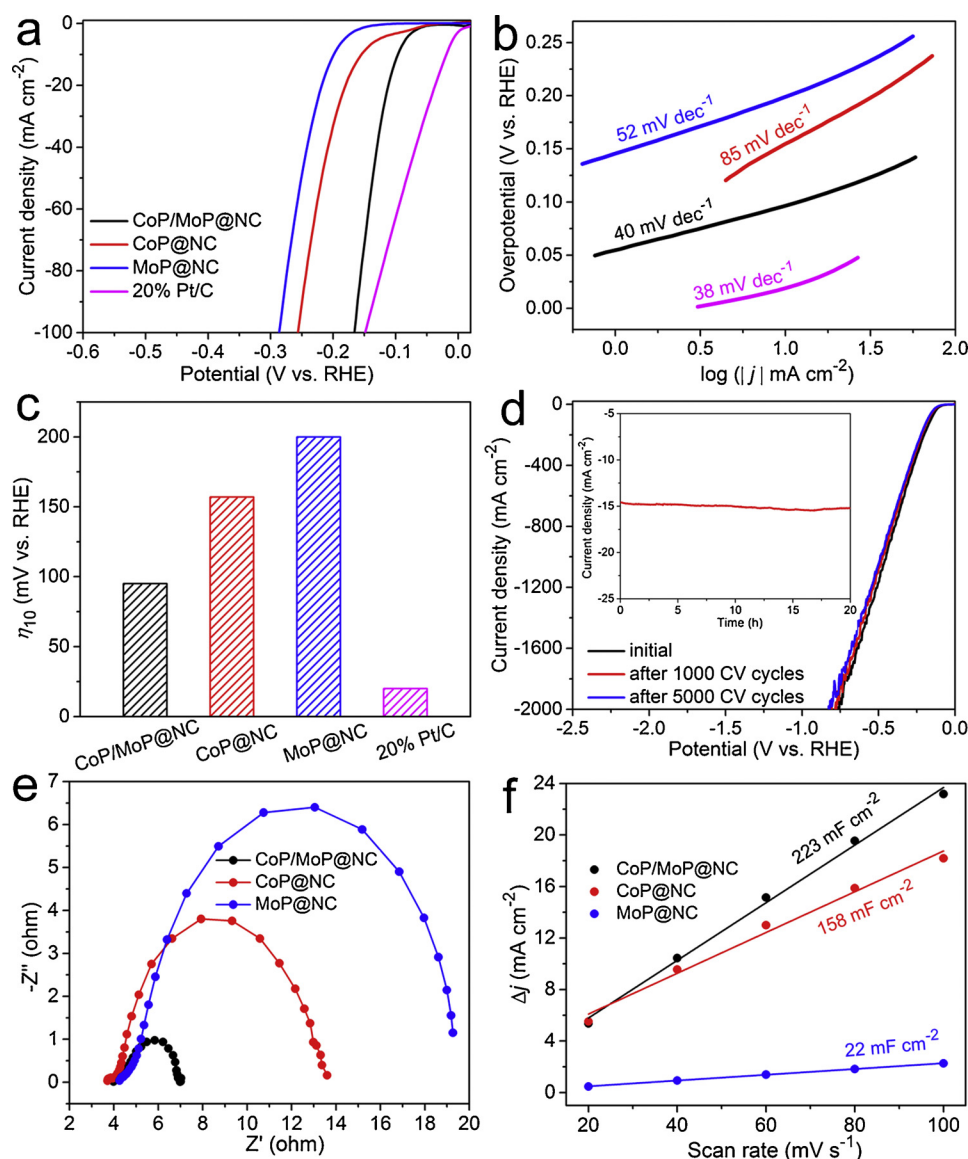


Fig. 4. (a) HER polarization curves, (b) Tafel slopes and (c) histogram of overpotentials at 10 mA cm^{-2} for CoP/MoP@NC, CoP@NC, MoP@NC and 20% Pt/C on CC substrate measured in 1 M KOH. (d) HER polarization curves of CoP/MoP@NC before and after 1000 and 5000 CV cycles, inset is chronopotentiometric curve. (e) EIS spectra recorded at the overpotential of 150 mV vs. RHE for HER. (f) C_{dl} calculations of CoP/MoP@NC, CoP@NC, MoP@NC.

efficient electrocatalyst to decrease the overpotential for high performance. As shown in Fig. 5a. LSV curves of CoP/MoP@NC and CoP@NC are almost overlapped with similar onset overpotentials and vertically increased current densities. In contrast, LSV curves of MoP@NC and commercial IrO_2 demonstrate poorer onset overpotentials and smaller current densities than CoP/MoP@NC. Tafel slope of CoP/MoP@NC (Fig. 5b) is only 81 mV dec^{-1} , which is smaller than that of the contrast samples (82 mV dec^{-1} for CoP@NC, 97 mV dec^{-1} for MoP@NC) and even lower than IrO_2 catalyst (94 mV dec^{-1}). The histogram (Fig. 5c) indicates that η_{10} of CoP/MoP@NC is only 270 mV vs. RHE, which is equal to CoP@NC, and much smaller than that of MoP@NC (420 mV) and IrO_2 (330 mV). Therefore, the required η_{10} and Tafel slope of CoP/MoP@NC are not only the lowest among these contrast samples but also comparable among recently reported phosphide-based electrocatalysts for OER, such as NiCoP (η_{10} , 280 mV; Tafel slope, 87 mV dec^{-1}) [53] and NiCoP@Cu₃P (η_{10} , 309 mV; Tafel slope, 42 mV dec^{-1}) [50] (Table S3).

Stability is very vital to evaluate OER performance of a catalyst. LSV curves before and after 1000 and even 5000 CV cycles (Fig. 5d) show nearly no decrease of the current density even reaching to the ultra-

high current density of 1000 mA cm^{-2} at the overpotential of 657 mV. CA curve of CoP/MoP@NC (inset Fig. 5d) demonstrates that the stable current density of ca. 10 mA cm^{-2} maintains 104% after continuous operation for 20 h at the overpotential of 300 mV. EIS spectra measured at the overpotential of 300 mV for OER are also used to analysis the electrocatalytic kinetics (Figure S14). R_{ct} of CoP/MoP@NC, CoP@NC and MoP@NC are 19.2, 21.5 and 2029Ω , respectively, suggesting the fast electron transfer of CoP/MoP@NC, which is in accord with their OER properties.

CoP/MoP@NC/CC electrode after 20 h CA test for HER and OER was studied by SEM, PXRD and XPS characterizations to understand the real active species for electrocatalysis. SEM image of CoP/MoP@NC/CC (Figure S15a) after CA test for HER suggests that the small-sized phosphide particles are well maintained. In contrast, SEM image (Figure S15b) after OER stability test shows emerging thin nanosheets on the surface of CoP/MoP@NC particles. PXRD spectrum of CoP/MoP@NC/CC (Figure S16) after OER stability occurs new peaks with high intensity, which can be assigning to Co(OH)_2 (JCPDS No. 3-913). Furthermore, detailed Co 2p XPS spectrum (Figure S17a) of CoP/MoP@NC/CC after OER stability still exhibits the existence of Co^{2+} and Co^{3+}

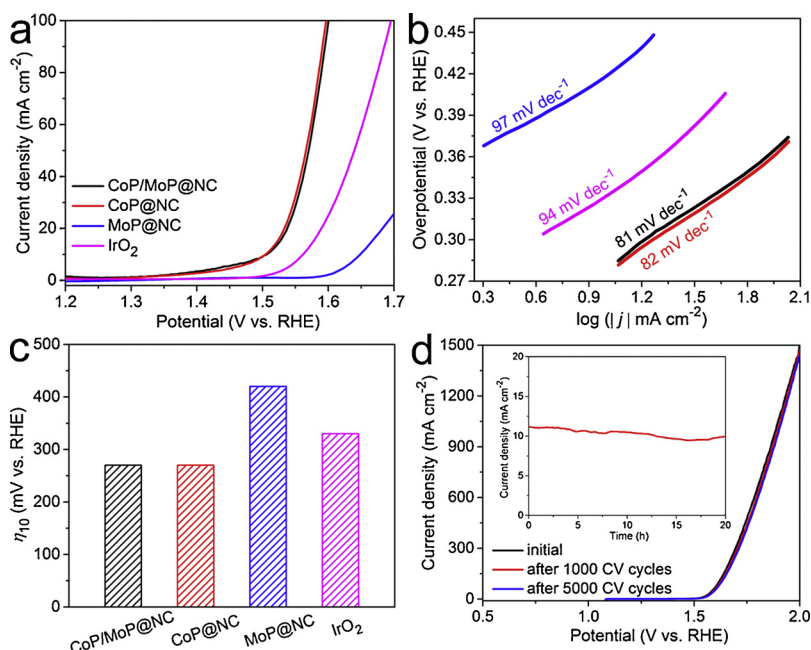


Fig. 5. (a) OER polarization curves, (b) Tafel slopes and (c) histogram of overpotentials at 10 mA cm⁻² for CoP/MoP@NC, CoP@NC, MoP@NC and IrO₂ on CC substrate measured in 1 M KOH. (d) OER polarization curves of CoP/MoP@NC before and after 1000 and 5000 CV cycles, inset is chronopotentiometric curve.

together with the satellite peaks. However, Co²⁺ peaks in Co 2p_{3/2} and Co 2p_{5/2} regions become relatively broad, suggesting the formation of Co(OH)₂ nanosheets on the surface. A new Co³⁺ peak in Co 2p_{1/2} region and enhanced Co³⁺ peak in Co 2p_{3/2} region can be associated with the as-formed CoOOH. [54]. After OER stability, Mo 3d XPS spectrum (Figure S17b) shows that the two Mo⁶⁺ peaks are disappeared and Mo⁴⁺ peaks become relatively strong, indicating the partial surface oxidation of MoP to MoO_x species [55]. In contrast, P 2p and N 1s spectra (Figure S17c, d) display the same species comparing with the XPS spectra before measurement. All these results indicate that the hydroxide and oxide species are newly formed on the surface of CoP/MoP@NC/CC during the catalytic process, which could be the active species for further improving the OER performance of phosphide-based composite in alkaline medium [18]. The phenomenon of the formation of hydroxides or oxides is usually observed by many reported transition metal-based OER electrocatalysts, such as phosphides [56] and sulfides [57].

3.2.3. Overall water splitting performance of CoP/MoP@NC/CC

Benefitting from the outstanding activities of both HER and OER, CoP/MoP@NC/CC can be utilized for overall water splitting [58,59]. Although the η₁₀ of CoP@NC is the same to that of CoP/MoP@NC, CoP@NC is still not suitable as the anode due to the poor OER stability (Figure S18). Fig. 6a is the photograph of the two-electrode device with CoP/MoP@NC/CC as both cathode and anode, which is denoted as CoP/MoP@NC||CoP/MoP@NC. As the cell voltage increases, lots of

bubbles are released simultaneously from cathode (H₂) and anode (O₂) (Video S1). Impressively, based on the LSV curves in Fig. 6b, a low cell voltage of 1.71 V is obtained at the high current density of 50 mA cm⁻² for CoP/MoP@NC||CoP/MoP@NC, which is in accord with the voltage difference (ΔV) between HER and OER at 50 mA cm⁻² (476 mV). Such a low voltage is even lower than the commercial 20% Pt/C||IrO₂ (1.74 V) and other contrast samples including CoP@NC||CoP@NC (1.77 V) and MoP@NC||MoP@NC (1.91 V). Moreover, the overall water splitting performance of CoP/MoP@NC/CC is comparable to most of recently phosphide-based electrocatalysts (Table S4). The outperformed activity of CoP/MoP@NC composite must result from the accessible pores and exposed active sites for rapid electrolyte diffusion and gas escape.

4. Conclusions

In summary, a new solid-phase hot-pressing method is applied to prepare POMs-ZIFs precursor on CC and their derived phosphide of CoP/MoP@NC/CC. Comparing with the traditional solvent method, this novel method possesses many advantages of rapidity, non-pollution and high yield. The synergistic effect of MoP, CoP and the as-formed surface oxide/hydroxide layers has a major impact on improving the electrocatalytic water splitting performance. The η₁₀ and Tafel slopes of CoP/MoP@NC/CC are 94 mV and 40 mV dec⁻¹ for HER and 270 mV and 81 mV dec⁻¹ for OER in 1 M KOH, respectively, which are one of the best performed phosphide-based electrocatalysts to date. In

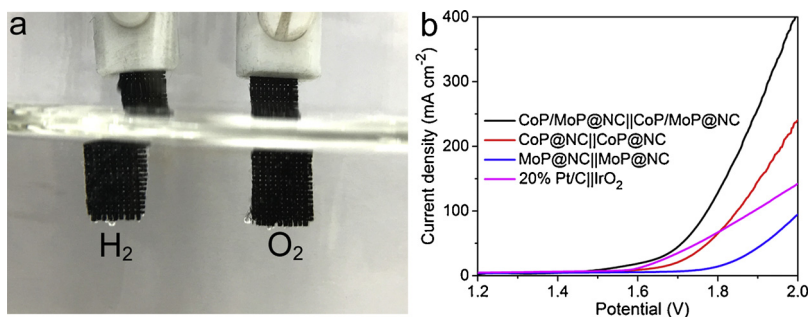


Fig. 6. Photograph of electrodes and the overall water splitting device in a two-electrode system. (b) LSV curves for overall water splitting of CoP/MoP@NC||CoP/MoP@NC, CoP@NC||CoP@NC, MoP@NC||MoP@NC and 20% Pt/C||IrO₂.

particular, the ultra-high current density (1000 mA cm^{-2}) can be reached at the low overpotentials (*i.e.*, 475 mV for HER, 657 mV for OER). When used as both cathode and anode for an overall water electrolyzer, CoP/MoP@NC/CC obtains the current density of 50 mA cm^{-2} at a low cell voltage of 1.71 V. This work exhibits an interesting perspective on preparing fast nucleating and stable MOFs and other nanomaterials using this efficient solid-phase hot-pressing method and applying to the renewable energy applications.

Acknowledgements

This work was financially supported by NSFC (No. 21622104, 21871141, 21871142 and 21701085), the NSF of Jiangsu Province of China (No. SBK2017040708), the Natural Science Research of Jiangsu Higher Education Institutions of China (No. 17KJB150025), Priority Academic Program Development of Jiangsu Higher Education Institutions and the Foundation of Jiangsu Collaborative Innovation Center of Biomedical Functional Materials.

Appendix A. Supplementary data

Supplementary material related to this article can be found, in the online version, at doi:<https://doi.org/10.1016/j.apcatb.2019.01.007>.

References

- [1] R. Detchon, L.R. Van, *Nature* 508 (2014) 309–311.
- [2] J.A. Turner, *Science* 305 (2004) 972–974.
- [3] H.B. Gray, *Nat. Chem.* 1 (2009) 7–7.
- [4] D.R. Palo, R.A. Dagle, J.D. Holladay, *Chem. Rev.* 107 (2007) 3992–4021.
- [5] Y. Zheng, Y. Jiao, M. Jaroniec, S.Z. Qiao, *Angew. Chem. Int. Ed.* 54 (2015) 52–65.
- [6] Z.W. Seh, J. Kibsgaard, C.F. Dickens, I. Chorkendorff, J.K. Nørskov, T.F. Jaramillo, *Science* 355 (2017) ead4998.
- [7] C.G. Moralesguio, L.A. Stern, X. Hu, *Chem. Soc. Rev.* 45 (2015) 6555–6569.
- [8] C.C.L. McCrory, S. Jung, J.C. Peters, T.F. Jaramillo, *J. Am. Chem. Soc.* 135 (2013) 16977–16987.
- [9] D.C. de Oliveira, W.O. Silva, M. Chatenet, F.H.B. Lima, *Appl. Catal. B-Environ.* 201 (2017) 22–28.
- [10] J.-X. Feng, J.-Q. Wu, Y.-X. Tong, G.-R. Li, *J. Am. Chem. Soc.* 140 (2018) 610–617.
- [11] J. Yin, Y. Li, F. Lv, M. Lu, K. Sun, W. Wang, L. Wang, F. Cheng, Y. Li, P. Xi, S. Guo, *Adv. Mater.* 29 (2017) 1704681.
- [12] R. Miao, B. Dutta, S. Sahoo, J. He, W. Zhong, S.A. Cetegen, T. Jiang, S.P. Alpay, S.L. Suib, *J. Am. Chem. Soc.* 139 (2017) 13604–13607.
- [13] Z. Lai, A. Chaturvedi, Y. Wang, T.H. Tran, X. Liu, C. Tan, Z. Luo, B. Chen, Y. Huang, G.-H. Nam, Z. Zhang, Y. Chen, Z. Hu, B. Li, S. Xi, Q. Zhang, Y. Zong, L. Gu, C. Kloc, Y. Du, H. Zhang, *J. Am. Chem. Soc.* 140 (2018) 8563–8568.
- [14] C. Tan, Z. Luo, A. Chaturvedi, Y. Cai, Y. Du, Y. Gong, Y. Huang, Z. Lai, X. Zhang, L. Zheng, X. Qi, M.H. Goh, J. Wang, S. Han, X.-J. Wu, L. Gu, C. Kloc, H. Zhang, *Adv. Mater.* 30 (2018) 1705509.
- [15] H. Xu, Z.X. Shi, Y.X. Tong, G.R. Li, *Adv. Mater.* 30 (2018) 1705442.
- [16] Y.-Q. Zhang, M. Li, B. Hua, Y. Wang, Y.-F. Sun, J.-L. Luo, *Appl. Catal. B-Environ.* 236 (2018) 413–419.
- [17] A.B. Laursen, R.B. Wexler, M.J. Whitaker, E.J. Izett, K.U.D. Calvino, S. Hwang, R. Rucker, H. Wang, J. Li, E. Garfunkel, M. Greenblatt, A.M. Rappe, G.C. Dismukes, *ACS Catal.* 8 (2018) 4408–4419.
- [18] K. Liu, F. Wang, P. He, T.A. Shifa, Z. Wang, Z. Cheng, X. Zhan, J. He, *Adv. Energy Mater.* 8 (2018) 1703290.
- [19] C. Luan, G. Liu, Y. Liu, L. Yu, Y. Wang, Y. Xiao, H. Qiao, X. Dai, X. Zhang, *ACS Nano* 12 (2018) 3875–3885.
- [20] Y. Jin, S. Huang, X. Yue, H. Du, P.K. Shen, *ACS Catal.* 8 (2018) 2359–2363.
- [21] P. Li, X. Duan, Y. Kuang, Y. Li, G. Zhang, W. Liu, X. Sun, *Adv. Energy Mater.* 8 (2018) 1703341.
- [22] L.-A. Stern, L. Feng, F. Song, X. Hu, *Energy Environ. Sci.* 8 (2015) 2347–2351.
- [23] Y. Tan, H. Wang, P. Liu, Y. Shen, C. Cheng, A. Hirata, T. Fujita, Z. Tang, M. Chen, *Energy Environ. Sci.* 9 (2016) 2257–2261.
- [24] E.J. Popczun, J.R. McKone, C.G. Read, A.J. Baciocchi, A.M. Wiltrout, N.S. Lewis, R.E. Schaak, *J. Am. Chem. Soc.* 135 (2013) 9267–9270.
- [25] D. Li, H. Baydoun, B. Kulikowski, S.L. Brock, *Chem. Mater.* 29 (2017) 3048–3054.
- [26] J. Tian, Q. Liu, A.M. Asiri, X. Sun, *J. Am. Chem. Soc.* 136 (2014) 7587–7590.
- [27] S. Fu, C. Zhu, J. Song, M. Engelhard, X. Li, D. Du, Y. Lin, *ACS Energy Lett.* 1 (2016) 792–796.
- [28] B.K. Kim, S.-K. Kim, S.K. Cho, J.J. Kim, *Appl. Catal. B-Environ.* 237 (2018) 409–415.
- [29] H.-W. Liang, S. Brüller, R. Dong, J. Zhang, X. Feng, K. Müllen, *Nat. Commun.* 6 (2015) 7992.
- [30] H. Furukawa, K.E. Cordova, M. O’Keeffe, O.M. Yaghi, *Science* 341 (2013) 1230444.
- [31] M. Zhao, Y. Huang, Y. Peng, Z. Huang, Q. Ma, H. Zhang, *Chem. Soc. Rev.* 47 (2018) 6267–6295.
- [32] Z. Liang, C. Qu, D. Xia, R. Zou, Q. Xu, *Angew. Chem. Int. Ed.* 130 (2018) 9750–9780.
- [33] Y.V. Kaneti, J. Tang, R.R. Salunkhe, X. Jiang, A. Yu, K.C.W. Wu, Y. Yamauchi, *Adv. Mater.* 29 (2017) 1604898.
- [34] X. Cao, C. Tan, M. Sindoro, H. Zhang, *Chem. Soc. Rev.* 46 (2017) 2660–2677.
- [35] F. Cao, M. Zhao, Y. Yu, B. Chen, Y. Huang, J. Yang, X. Cao, Q. Lu, X. Zhang, Z. Zhang, C. Tan, H. Zhang, *J. Am. Chem. Soc.* 138 (2016) 6924–6927.
- [36] R. Zhang, X.Y. Dong, J. Du, J.Y. Zhao, S.Q. Zang, *Adv. Mater.* 30 (2017) 1703711.
- [37] J. Yang, F. Zhang, X. Wang, D. He, G. Wu, Q. Yang, X. Hong, Y. Wu, Y. Li, *Angew. Chem. Int. Ed.* 128 (2016) 13046–13050.
- [38] Y. Xu, W. Tu, B. Zhang, S. Yin, Y. Huang, M. Kraft, R. Xu, *Adv. Mater.* 29 (2017) 1605957.
- [39] Y.-J. Tang, Y. Chen, H.-J. Zhu, A.M. Zhang, X.-L. Wang, L.-Z. Dong, S.-L. Li, Q. Xu, Y.-Q. Lan, *J. Mater. Chem. A* 6 (2018) 21969–21977.
- [40] Y. Pan, K. Sun, S. Liu, X. Cao, K. Wu, W.-C. Cheong, Z. Chen, Y. Wang, Y. Li, Y. Liu, D. Wang, Q. Peng, C. Chen, Y. Li, *J. Am. Chem. Soc.* 140 (2018) 2610–2618.
- [41] H. Zhang, S. Hwang, M. Wang, Z. Feng, S. Karakalos, L. Luo, Z. Qiao, X. Xie, C. Wang, D. Su, Y. Shao, G. Wu, *J. Am. Chem. Soc.* 139 (2017) 14143–14149.
- [42] D.-L. Long, R. Tsunashima, L. Cronin, *Angew. Chem. Int. Ed.* 49 (2010) 1736–1758.
- [43] H. Yan, Y. Xie, Y. Jiao, A. Wu, C. Tian, X. Zhang, L. Wang, H. Fu, *Adv. Mater.* 30 (2018) 1704156.
- [44] H. Yan, C. Tian, L. Wang, A. Wu, M. Meng, L. Zhao, H. Fu, *Angew. Chem. Int. Ed.* 54 (2015) 6325–6329.
- [45] H. Yan, Y. Jiao, A. Wu, C. Tian, X. Zhang, L. Wang, Z. Ren, H. Fu, *Chem. Commun.* 52 (2016) 9530–9533.
- [46] Y.-Y. Ma, Z.-L. Lang, L.-K. Yan, Y.-H. Wang, H.-Q. Tan, K. Feng, Y.-J. Xia, J. Zhong, Y. Liu, Z.-H. Kang, Y.-G. Li, *Energy Environ. Sci.* 11 (2018) 2114–2123.
- [47] C. Chen, A. Wu, H. Yan, Y. Xiao, C. Tian, H. Fu, *Chem. Sci.* 9 (2018) 4746–4755.
- [48] K. Zhou, B. Mousavi, Z. Luo, S. Phatanasri, S. Chaemchuen, F. Verpoort, *J. Mater. Chem. A* 5 (2016) 952–957.
- [49] L. Yan, L. Cao, P. Dai, X. Gu, D. Liu, L. Li, Y. Wang, X. Zhao, *Adv. Funct. Mater.* 27 (2017) 1703455.
- [50] X. Ma, Y. Chang, Z. Zhang, J. Tang, *J. Mater. Chem. A* 6 (2018) 2100–2106.
- [51] J. Song, C. Zhu, B.Z. Xu, S. Fu, M.H. Engelhard, R. Ye, D. Du, S.P. Beckman, Y. Lin, *Adv. Energy Mater.* 7 (2017) 1601555.
- [52] Y. Chen, G. Yu, W. Chen, Y. Liu, G.-D. Li, P. Zhu, Q. Tao, Q. Li, J. Liu, X. Shen, H. Li, X. Huang, D. Wang, T. Asefa, X. Zou, *J. Am. Chem. Soc.* 139 (2017) 12370–12373.
- [53] H. Liang, A.N. Gandi, D.H. Anjum, X. Wang, U. Schwingenschlög, H.N. Alshareef, *Nano Lett.* 16 (2016) 7718–7725.
- [54] K. Liu, C. Zhang, Y. Sun, G. Zhang, X. Shen, F. Zou, H. Zhang, Z. Wu, E.C. Wegener, C.J. Taubert, *ACS Nano* 12 (2017) 158–167.
- [55] Y. Jiang, Y. Lu, J. Lin, X. Wang, Z. Shen, *Small Methods* 2 (2018) 1700369.
- [56] F. Yu, H. Zhou, Y. Huang, J. Sun, F. Qin, J. Bao, W.A. Goddard III, S. Chen, Z. Ren, *Nat. Commun.* 9 (2018) 2551.
- [57] X. Zou, Y. Liu, G.-D. Li, Y. Wu, D.-P. Liu, W. Li, H.-W. Li, D. Wang, Y. Zhang, X. Zou, *Adv. Mater.* 29 (2017) 1700404.
- [58] P. Barbaro, F. Liguori, *Chem. Rev.* 109 (2009) 515–529.
- [59] A. Wu, Y. Xie, H. Ma, C. Tian, Y. Gu, H. Yan, X. Zhang, G. Yang, H. Fu, *Nano Energy* 44 (2018) 353–363.